Check for updates

A 3-D Printed Optically Clear Rigid Diseased Carotid Bifurcation Arterial Mock Vessel Model for Particle Image Velocimetry Analysis in Pulsatile Flow

Nicholas Stanley
Department of Engineering Technology and Construction Management (ETCM),
University of North Carolina at Charlotte,
9201 University City Blvd,
Charlotte, NC 28214
e-mail: nick.stanley615@gmail.com

Ashley Ciero
Department of Engineering Technology and Construction Management (ETCM),
Applied Energy and Electromechanical Engineering (AEES),
University of North Carolina at Charlotte,
9201 University City Blvd,
Charlotte, NC 28214
e-mail: akciero@gmail.com

William Timms
Department of Mechanical Engineering and Engineering Science (MEES),
University of North Carolina at Charlotte,
9201 University City Blvd,
Charlotte, NC 28214
e-mail: wtimms94@gmail.com

Rodward L. Hewlin Jr.[1]
Department of Engineering Technology and Construction Management (ETCM),
Center for Biomedical Engineering and Science (CBES),
University of North Carolina at Charlotte,
9201 University City Blvd,
Charlotte, NC 28214
e-mail: rhewlin@uncc.edu

In recent years, blood flow analyses of diseased arterial mock vessels using particle image velocimetry (PIV) have been hampered by the inability to fabricate optically clear anatomical vessel models that realistically replicate the complex morphology of arterial vessels and provide highly resolved flow images of flow tracer particles. The aim of this paper is to introduce a novel approach for producing optically clear 3-D printed rigid anatomical arterial vessel models that are suitable for PIV analysis using a common 3-D inkjet printing process (using a Formlabs Form 2 3-D printer) and stock clear resin (RS-F2-GPCL-04). By matching the index of refraction (IOR) of the working fluid to the stock clear resin material, and by printing the part in a 45-deg print orientation, a clear anatomical model that allows clear visualization of flow tracer particles can be produced which yields highly resolved flow images for PIV analyses. However, a 45-deg print orientation increases the need for post-processing due to an increased amount of printed support material. During post-processing, the part must be wet sanded in several steps and surface finished with Novus Plastic Polish 3 Step System to achieve the final surface finish needed to yield high-resolution flow images. The mock arterial vessel model produced in this work is a 3-D printed diseased carotid bifurcation artery developed from CTA scan data. A PIV analysis was conducted on the developed mock arterial vessel model installed in a complex transient flow loop to assess the flow profiles within the model and the clarity of the model. A computational fluid dynamics (CFD) simulation was conducted on the same carotid bifurcation arterial geometry, and the results were used as a benchmark comparison for PIV results. The results obtained in this work show excellent promise for using the developed approach for developing 3-D printed anatomical vessel models for experimental PIV analyses. The fabrication methodology of the clear anatomical models, PIV results, and CFD results is described in detail. [DOI: 10.1115/1.4056639]

Keywords: anatomical models, blood flow, carotid bifurcation, computational fluid dynamics (CFD), optically clear, particle image velocimetry (PIV), and 3-D printing., additive manufacturing, bioengineering, bioresearch, biofluid dynamics, biomedical, fluid mechanics/dynamics, instrumentation and components

1 Introduction

Cardiovascular disease continues to be the leading cause of death worldwide [1–4]. Experimental fluid dynamics has played a vital role in investigating pulsatile blood flow characteristics in vitro using mock arterial vessels to provide insight into the disease condition, disease progression, and design optimization of medical stents for disease intervention [5–11]. In-vitro studies use a physical representation of a diseased or stented artery with the goal of obtaining hemodynamic parametric data [12]. Particle image velocimetry (PIV) has been used extensively as a tool in in-vitro studies to noninvasively obtain hemodynamic parametric data for diseased artery cases and stented artery cases. However, one of the key limitations involving this approach is the need to produce quality images to resolve the flow characteristics of the artery being analyzed [13]. Some of the causes of poor image quality are due to laser glare and scattering light from the mock arterial vessel, inappropriate index of refraction (IOR) matching of the working fluid to the vessel material, the need for a bandpass filter, and artery models that lack optical transparency.

There are many methods for manufacturing mock arterial vessels for PIV analyses. The most common approach involves fabricating the mock artery model with a silicone elastomer using a lost casting technique [14–18]. This process is very time laborious, often suffers poor transparency due to voids formed in the material during casting under vacuum, and requires casting a mold in addition to a transparency box to house the artery and working fluid to achieve the same IOR as the artery material [19]. Recent advances in in-vitro arterial

[1]Corresponding author.

Manuscript received November 9, 2022; final manuscript received January 2, 2023; published online January 27, 2023. Assoc. Editor: Kwang-Yong Kim.

Copyright © 2023 by ASME; reuse license CC-BY 4.0

Downloaded from http://heattransfer.asmedigitalcollection.asme.org/openengineering/article-pdf/doi/10.1115/1.4056639/6977727/aoje_2_021010.pdf by guest on 19 July 2024

flow analysis using lost casting fabrication techniques of complex optically transparent arterial vessels have minimized some of the limitations mentioned.

In some cases, distortions due to IOR mismatch have been accounted for using image correction and/or dewarping techniques. Performing these techniques is often difficult for basic models and impossible for complex arterial models with varying diameters and branching. IOR matching is often a preferred method to avoid time-consuming code development for image correction and added accessories to the PIV camera [20]. As a result, in-vitro experiments may be conducted with inexpensive in-house developed working fluid mixtures such as distilled water and glycerol [21,22].

Although few studies have been reported, some studies have reported that 3-D printing may be used to fabricate optically clear vessels suitable for PIV analyses [23–26]. These studies have reported that optimal transparency is best achieved when printing the model normal to the print plane, as opposed to printing in the direction of print layering. The present work aims to build on previous work and fabricate an optically clear arterial model of a patient-specific carotid artery model using 3-D printing. The overall goal of this paper is to verify that 3-D printing may be used as a viable rapid prototyping tool for fabricating optically clear rigid arterial vessels for PIV analysis and summarize the fabrication methodology.

2 Methodology

2.1 3-D Printing and Post-Processing Methodology. In the efforts of evaluating the practicality of using 3-D printed anatomical vessels for PIV analyses, an initial square extrusion test sample incorporating a hollow circular conduit for fluid and particle tracer flow is shown in Fig. 1. The test sample was developed in Solidworks™ v19 CAD software. The test sample was printed using a desktop Formlabs Form 2 3-D printer and stock clear resin (RS-F2-GPCL-04). The test samples were printed in a 45-deg build-plane orientation as shown in Fig. 1(*b*). Figure 2

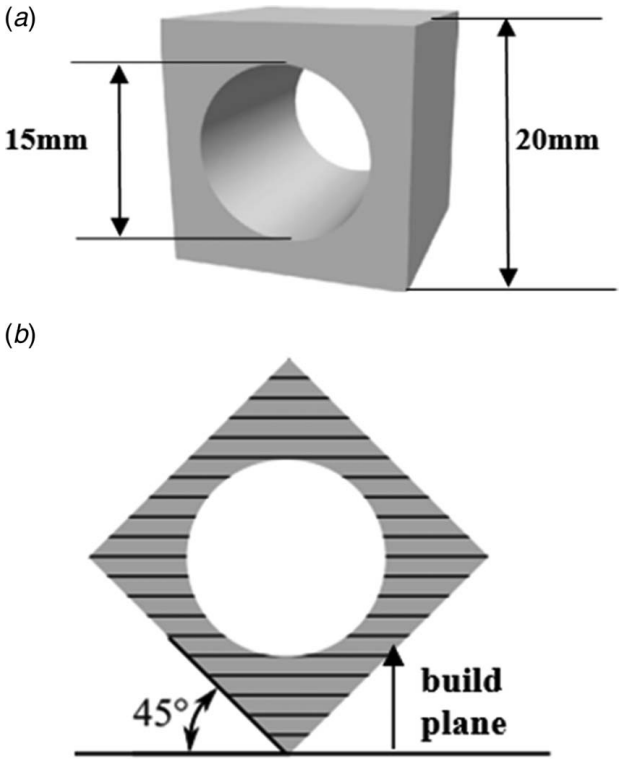

Fig. 1 CAD model of 3-D printed test models: (*a*) isometric view and (*b*) front view positioned 90 deg from the build plane and 45 deg from the build plane

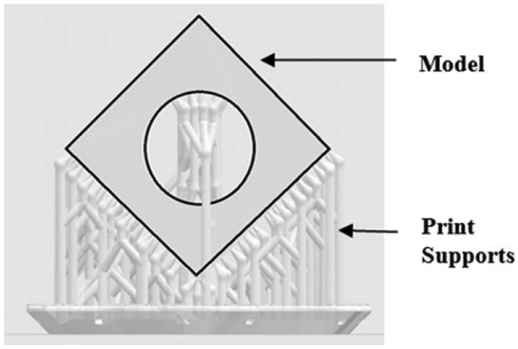

Fig. 2 Slicer model of the test sample in a 45-deg orientation with print supports. The cube face edges are bolded in black to outline the geometry

provides an illustration of the square extrusion modeled with the support material in slicer software prior to 3-D printing. For 3-D printing, the print settings were set to the finest print resolutions setting, resulting in a print layer resolution of 25 μm (0.001 in.). The print support material was removed (cutoff) and then soaked in an isopropyl alcohol solution for 20 min to remove the additional undesired resin. Additional post-processing was then done in the following steps:

(1) The test sample was first placed on a motorized rotary apparatus and exposed to an ultraviolet (UV) light source to cure the resin over a 24-h period.
(2) The outer surface of the test samples was then wet sanded perpendicular to the print layers with coarse grit sandpaper and incrementally progressed to finer grit sandpaper (P600-P2000).
(3) Each surface was sanded for approximately 30 min. A honing tool was used to sand the flow conduit. The sanding process was timed to improve the uniformity of resin material removal.
(4) Each surface was inspected under a bright light source between and after sanding steps. Sanding of each surface was repeated for an additional 30 min until layering or surface defects from the previous sanding passes were no longer visible. The total sanding time was 1 h.
(5) Finally, the surfaces were polished with a micro cloth and a three-step polishing compound (NOVUS Plastic Polish; Novus Inc., St. Paul, MN) to obtain a transparent finish on the 3-D printed sample.

2.2 Test Sample Particle Image Velocimetry Analysis Methodology. For PIV analyses, the test sample was illuminated by a 1.0-mm-thick laser light sheet provided by a pulse Nd:YAG Solo III Laser by New Wave Research outfitted with a laser optic and focal lens. The test sample was filled with a working fluid composed of sodium iodide (NaI), glycerol, sodium thiosulfate, and distilled water mixture to match the IOR of the Formlabs stock clear resin (IOR was reported to be 1.5304 [27]).

Fluorescent polymer microspheres (Fluoro-Max 36-3B; Thermo Scientific Inc., Fremont, CA) were added to the fluid to serve as tracer particles. Images were recorded with a Flare 12MP high-speed CMOS camera outfitted with a Nikkon AF Micro-Nikkor 60 mm f/2.8D objective and long pass filter (Edmund Optics). A 1TB DVR core (DVR Express Core 2) was used to store raw images. Tracer particle flow images were resolved using PIVLab, an open-source MATLAB-based PIV software. The PIV system was calibrated using a simple gravity-driven flow system setup with an elevated tank open to the atmosphere to supply the working fluid through the piping to the test-section sample. The fluid exited the system through a restricted orifice and flowed into a beaker. A CAD model schematic is shown in Fig. 3.

Downloaded from http://heattransfer.asmedigitalcollection.asme.org/openengineering/article-pdf/doi/10.1115/1.4056639/6977727/aoje_2_021010.pdf by guest on 19 July 2024

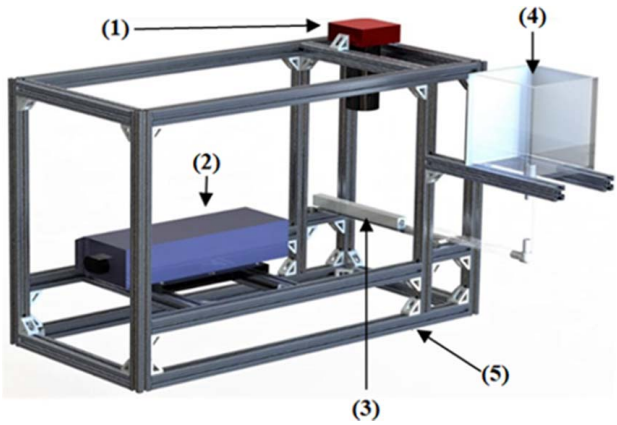

Fig. 3 PIV system and gravity-driven flow system setup: (1) camera, (2) laser, (3) test section, (4) tank, and (5) aluminum framing

The fluid volumetric level was monitored and timed with a stopwatch to obtain the average volumetric flowrate. The average velocity was calculated and used to obtain the theoretical velocity profile using the Poiseuille equation shown in Eq. (1)

$$u(r) = u_{avg}\left(1 - \left(\frac{r}{R}\right)^2\right) \tag{1}$$

where u_{avg} is the average velocity, r is the radius, and R is the maximum radius. During calibration, the PIV image resolution was determined to be approximately 32 μm per pixel. An image straddling technique was used in which a signal generator within the DVR core generated a 15 Hz square wave that fired the camera shutter. The camera was set to capture images in double exposure and set to 30 Hz with a first frame exposure of 500 μs to synchronize with the laser pulses. The laser system was fired based on the generated square wave at a delay of 250 μs and 750 μs for the first and second lasers, respectively.

After performing cross-correlation and image post-processing, the velocity data were averaged to obtain the mean velocity field contours as shown in Fig. 4(*b*). The flow was observed to be steady with relatively small variations in the velocity along the centerline as shown in Fig. 4(*b*). The theoretical velocity profile obtained from the Poiseuille solution (Eq. (1)) was compared to the velocity profile obtained from the PIV images as shown in Fig. 4(*c*). Standard deviations were calculated from the theoretical and PIV results and showed minimum error due to the clarity of the part. To demonstrate that the model is suitable for transient flow PIV analyses, a simple flow loop was assembled from 0.25 in. plastic tubing, barbed fittings, an inline flowmeter, clamp on flowmeter, a compliance chamber, a reservoir, a magnetic stirrer, and a custom pulsatile pump (BDC labs model PD-1100 Wheat Ridge, CO) to circulate flow from the reservoir to the test section. The tracer particles were dispersed into the flow loop at the reservoir and a magnetic stirrer was placed underneath the reservoir to stir a magnetic bar inside the reservoir to keep the particles evenly suspended and dispersed into the outgoing flow.

A simple sinusoidal volumetric waveform was implemented at the inlet with a peak volumetric magnitude of 1 L/min at a frequency of 60 bpm. An image of the velocity vector field and contours at the peak of the volumetric waveform is shown in Fig. 5. As shown in Fig. 5, a Womersley velocity profile is established in which the flow is highly skewed toward the upper wall. This is also shown in the extracted velocity profile as shown in Fig. 5. The velocity also appears to vary along the centerline of the test sample. As a comparison, the analytical Womersley solution was plotted as a benchmark for PIV results using MATLAB. The derivation of the Womersley solution is described in detail in the next section.

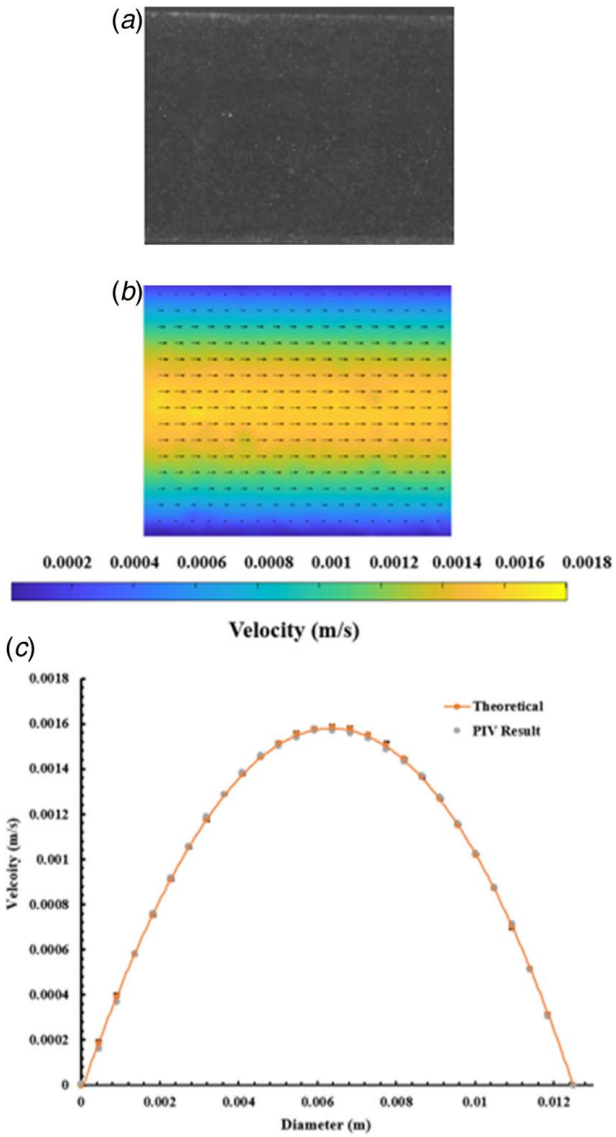

Fig. 4 Test sample PIV results: (*a*) PIV raw image, (*b*) PIV velocity vector and contour plot, and (*c*) velocity profile

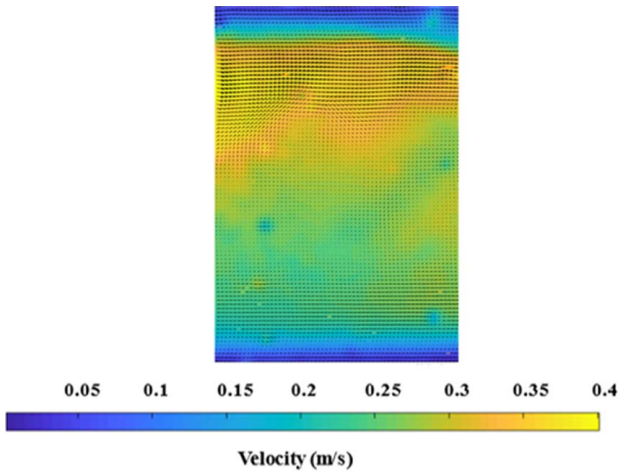

Fig. 5 Test sample transient PIV velocity contour results

Downloaded from http://heattransfer.asmedigitalcollection.asme.org/openengineering/article-pdf/doi/10.1115/1.4056639/6977727/aoje_2_021010.pdf by guest on 19 July 2024

2.3 Womersley Velocity Profile Solution Derivation. The Womersley velocity profiles for pulsating flow in straight pipes can be derived from the momentum equation for fully developed flow by using Bessel functions [28,29]. The momentum equation for fully developed flow in dimensionless form is described in Eq. (2)

$$\alpha^2 \frac{\partial u}{\partial t} = -\frac{\partial P}{\partial x} + \frac{1}{r}\frac{\partial}{\partial r}\left(r\frac{\partial u}{\partial r}\right) \tag{2}$$

in which the pressure derivative is the driving force of the flow and is described below

$$\frac{\partial P}{\partial x} = \frac{\partial \hat{P}}{\partial x} e^{i\varpi t} \tag{3}$$

The velocity is also oscillatory and written in the following form:

$$u = \hat{u} e^{i\varpi t} \tag{4}$$

substituting these relations back into the momentum equation (Eq. (3)) yields

$$i\varpi\alpha^2 \hat{u}(r) = -\frac{\partial \hat{P}}{\partial x} + \frac{1}{r}\frac{\partial}{\partial r}\left(r\frac{\partial \hat{u}}{\partial r}\right) \tag{5}$$

The Bessel equation for $n = 0$ is obtained by substituting $s = i^{2/3}\alpha r$ into Eq. (5). This equation is then rearranged as follows:

$$\frac{\partial^2 \hat{u}}{\partial s^2} + \frac{1}{s}\frac{\partial \hat{u}}{\partial s} + \left(1 - \frac{n^2}{s^2}\right)u = \frac{i}{\rho\omega}\frac{\partial \hat{P}}{\partial x} \tag{6}$$

The final solution can be expressed with Bessel functions $J_0(r)$

$$\hat{u} = \frac{i}{\rho\omega}\frac{\partial \hat{P}}{\partial z}\left(1 - \frac{J_0(i^{3/2}\alpha r/a)}{J_0(i^{3/2}\alpha)}\right) \tag{7}$$

From this expression, the numerical solution of Womersley profiles for straight pulsatile pipe flow is found by reintroducing $u = \hat{u}\, e^{i\omega t}$, in which the final form of the Womersley numerical solution is

$$u(r, t) = \mathrm{Re}\left[\frac{i}{\rho\omega}\frac{\partial \hat{P}}{\partial x} e^{i\omega t}\left(1 - \frac{J_0(i^{3/2}\alpha r/a)}{J_0(i^{3/2}\alpha)}\right)\right] \tag{8}$$

A MATLAB script file was written to solve the numerical Womersley solution in Eq. (8) over a total time of 5.8 s. Figure 6 shows a plot of the Womersley velocity profile solution at 5.8 s and the PIV velocity profile at 5.8 s. The next section discusses the printed mock carotid artery model fabrication methodology.

2.4 3-D Printed Mock Carotid Artery Model Fabrication. To demonstrate the feasibility of fabricating a more complex 3-D printed model for PIV, we considered in this work a patient-specific carotid bifurcation model used in our previous studies [30–34]. In preparation for 3-D printing, a negative of the carotid artery lumen was designed in Solidworks™ v19 CAD software. The negative consisted of a rectangular cross-section encompassing the vessel segments as shown in Fig. 7. The anatomical model was fabricated following the same procedure as outlined for the test-section printed part. The entire model was printed in a 45-deg build-plane orientation as shown in Fig. 7(*b*). The exterior of the arterial model was sanded and polished using the same steps as outlined previously. Unlike the test sample, the interior of the model was not post-processed.

It is worth mentioning that several characteristics of the 3-D printed mock carotid artery model in the present work complicate traditional fabrication approaches (e.g., using computer numerical controlled (CNC) milling): (1) both the internal carotid artery (ICA) and external carotid artery (ECA) branches are curved in the anteroposterior direction and (2) the vessel cross-sections are constantly varying in diameter along the centerline axis. Traditional fabrication techniques such as CNC milling would involve fabricating the model using acrylic and would also require splitting the model into two sections to machine the internal surface of the lumen and lastly fusing the two sections together for the final model. The mate seam created by this procedure would produce

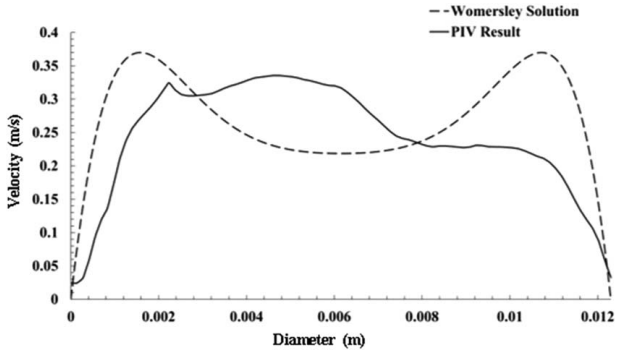

Fig. 6 Plot of the Womersley solution velocity profile and the PIV velocity profile at 5.8 s in the sinusoidal velocity waveform

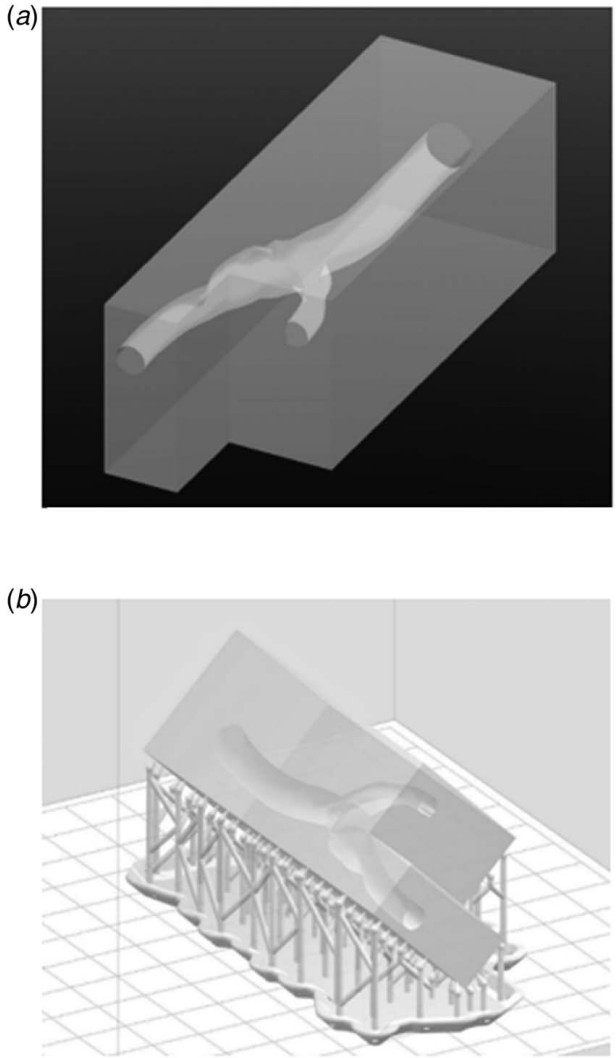

Fig. 7 Carotid artery anatomical: (*a*) CAD model and (*b*) slicer model with print supports

Downloaded from http://heattransfer.asmedigitalcollection.asme.org/openengineering/article-pdf/doi/10.1115/1.4056639/6977727/aoje_2_021010.pdf by guest on 19 July 2024

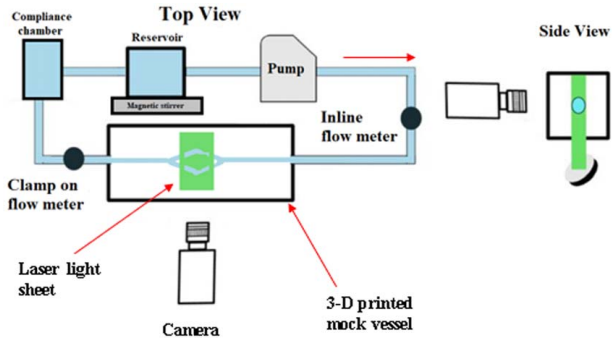

Fig. 8 Schematic diagram of the PIV and pulsatile flow loop setup for the 3-D printed mock arterial flow analysis experiments

issues such as restricting the laser light sheet and camera access for PIV raw image capture. Additionally, because of the varying curvature of the carotid artery model, a four-axis CNC mill would be required to accurately reproduce the model geometry, greatly increasing the cost of fabrication. The direct 3-D printing and post-processing approach presented in the present work overcomes these limitations. The next section discusses the PIV setup and methodology for conducting PIV analyses on the 3-D printed carotid artery mock vessel model developed in this work.

2.5 Arterial Model Particle Image Velocimetry Analysis Methodology. The same pulsatile flow loop used in the transient straight pipe test sample experiments was used for transient PIV analysis of the 3-D printed mock arterial vessel model. A schematic of the pulsatile flow loop with the 3-D printed mock carotid artery vessel model installed in the loop is shown in Fig. 8. Similar to the test sample, a clear 3-D printed section was glued and fastened to the arterial mock vessel model to satisfy the entrance length for fully developed flow. An additional 3-D printed y-shaped junction was added at the exits to merge the exiting fluid back to one pipe to be routed to the compliance chamber. A graphic of the mock carotid artery vessel model with the 3-D printed entrance and exit additions is shown in Fig. 9(*a*). Figure 9(*b*) shows the diseased section of the artery and the region of interest (ROI) in which PIV measurements are obtained.

For PIV experiments, the flow loop was operated over a period of 5 min prior to collecting data to ensure that the system transients (bubbles and other startup-unsteady flow effects) present in the

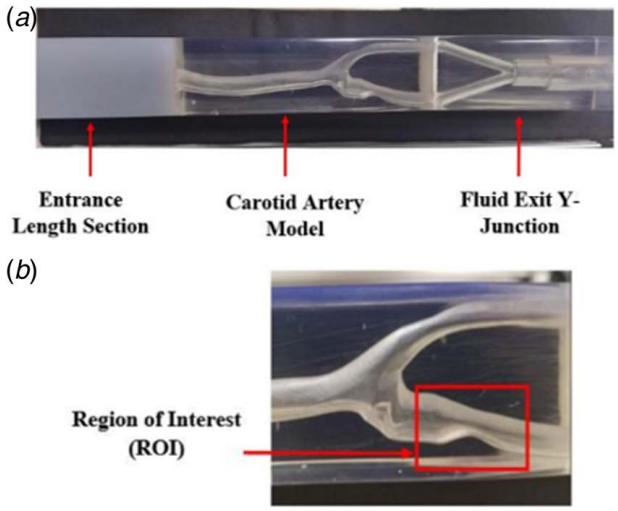

Fig. 9 3-D printed carotid bifurcation model: (*a*) fully assembled model with entrance and exit sections and (*b*) stenosis ROI

arterial model section were minimized/removed. The pump and PIV system were synchronized to record data in time with the periodicity of the pulsatile waveform. A simplified cardiac velocity waveform was used in the transient arterial PIV experiment to mimic cardiac flow. The waveform was written in the pulse duplicator's software as a piecewise unsteady velocity waveform. The piecewise velocity waveform is described in Eq. (9)

$$\bar{u}(t)=\begin{cases}83.33t^3-12.50t^2+0.21667t+0.13\\ 7517.12t^4-5688.27t^3+1529.70t^2-169.61t+6.6462\\ -96.923t^3+100.30t^2-34.425t+4.1629\\ 58.291t^2-5235.7t+1193\\ 18.835t^3-36.960t^2+23.427t-4.60\end{cases} \quad (9)$$

$$0\,\text{s}\le t\le 0.15\,\text{s}$$
$$0.15\,\text{s}\le t\le 0.24\,\text{s}$$
$$0.24\,\text{s}\le t\le 0.42\,\text{s}$$
$$0.42\,\text{s}\le t\le 0.47\,\text{s}$$
$$0.47\,\text{s}\le t<0.80\,\text{s}$$

In the efforts of assessing the optical clarity of the model and the validity of the extracted PIV velocity profile result at the ROI site of the mock artery vessel, a 3-D pulsatile computational fluid dynamics (CFD) simulation was conducted. The next section discusses the CFD modeling methodology.

2.6 Computational Fluid Dynamics Simulation Modeling Methodology. The flow simulation conducted in this work was performed in ANSYS Fluent™ 19. The continuity and three-dimensional Navier–Stokes equations describing pulsatile flow as an incompressible fluid are implemented and numerically solved in a finite volume formulation

$$\nabla\cdot u=0 \quad (10)$$

$$\rho\left(\frac{\partial u}{\partial t}+u(u\cdot\nabla)\right)=-\nabla P+\nabla\cdot(\mu\nabla u) \quad (11)$$

where u is the three-dimensional velocity vector, ρ is the density of blood, P is the pressure, and μ is the dynamic viscosity. The same piecewise unsteady velocity waveform (Eq. (9)) used in the transient PIV experiment is implemented at the inlet of the model. The unsteady inlet velocity is modeled as fully developed as shown in Eq. (12). The same piecewise velocity waveform used for the PIV analyses is modeled in the CFD simulations (Eq. (9)) as $\bar{u}$ in Eq. (12). The walls of the arterial vessel are modeled as rigid vessels with the no-slip condition applied at the boundary

$$u(y,\,t)=2\bar{u}(t)\left[1-\left(\frac{y}{R}\right)^2\right] \quad (12)$$

For meshing and grid independence, the flow domain was discretized into numerous tetrahedral computational cells. The arterial model was tested for three different mesh grid densities, i.e., 274, 548, and 1096 cells in the cross-sectional flow area. The time-averaged absolute difference in centerline axial velocity between the coarse and fine cross-sectional mesh was 2.2 mm/s, and that between fine and finer one was only 1 mm/s, which was very small relative to the mean centerline axial velocity value of 105 mm/s. The mesh scheme that contained 548 cells per cross-section, i.e., 230,608 for the whole arterial mesh is shown in Fig. 10. This mesh was evaluated over 80-time-steps per cycle and provided the best grid result for grid independence and stability in solutions within a satisfactory CPU time. Figure 10 also shows the boundary condition assignments.

The outlet pressures of the ECA and ICA are modeled using Windkessel boundary conditions. The Windkessel boundary conditions are expressed through an ordinary differential equation (ODE)

Downloaded from http://heattransfer.asmedigitalcollection.asme.org/openengineering/article-pdf/doi/10.1115/1.4056639/6977727/aoje_2_021010.pdf by guest on 19 July 2024

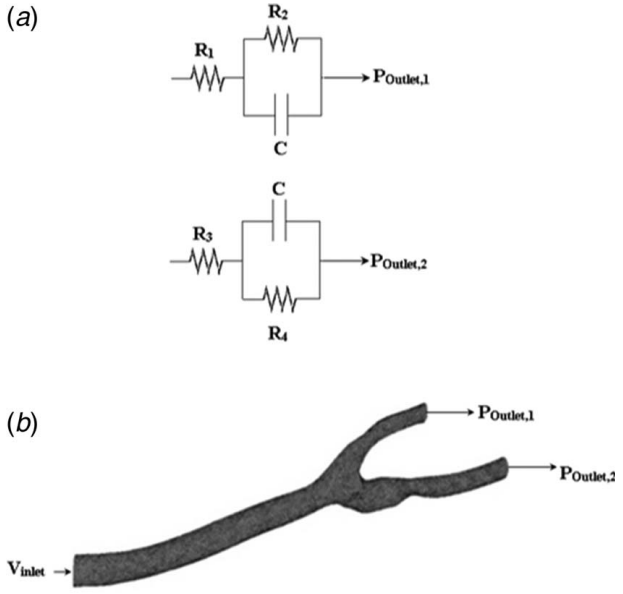

Fig. 10 Top view of the computational mesh and boundary conditions: (*a*) enlarged view of the electrical circuit describing the prescribed boundary conditions for the outlets and (*b*) the arterial computational mesh

Table 1 Resistance and capacitance values used for the Windkessel boundary conditions

	R_d (Pa s/m^3)	C (m^3/Pa)	R_p (Pa s/m^3)
ICA	1.11×10^{6}	4.20×10^{-13}	8.15×10^{11}
ECA	2.27×10^{6}	2.27×10^{-13}	4.07×10^{12}

Values obtained from the work of Gharahi et al. [42].

similar to the relation between voltage, current, and capacitance in electrical circuits. The ODE used for flow simulations is shown in Eq. (13), where R_p is the proximal resistance for large arteries and arterioles, R_d is the distal resistance for simulating small arterioles and capillaries, C is the vessel compliance for large arteries and arterioles, $i(t)$ represents the flowrate, and $P(t)$ is the time-dependent pressure. Table 1 lists the values used to model the Windkessel boundary conditions in this work

$$\left(1+\frac{R_p}{R_d}\right)i(t)+CR_d\frac{di(t)}{dt}=\frac{P(t)}{R_d}+C\frac{dP(t)}{dt} \tag{13}$$

Figure 11 shows a plot of the unsteady velocity waveform at the inlet of the carotid artery along with the resultant Windkessel pressure profile outputs at the outlet.

A user-defined function was written to compute the cardiac waveform over a period of five cycles. The user-defined function was compiled in the ANSYS Fluent platform for simultaneous flow calculations. A user-defined expression was used to implement the fully developed waveform in the equation. The Navier–Stokes equations were solved implicitly using a quadratic upwind discretization scheme (QUICK) for nonlinear terms. The next section presents the results obtained from this work.

3 Results

This paper presents a novel manufacturing approach for producing 3-D printed mock arterial vessel models for PIV analyses. This manufacturing technique has been implemented and tested via PIV and validated with the Womersley analytical solution and 3-D CFD

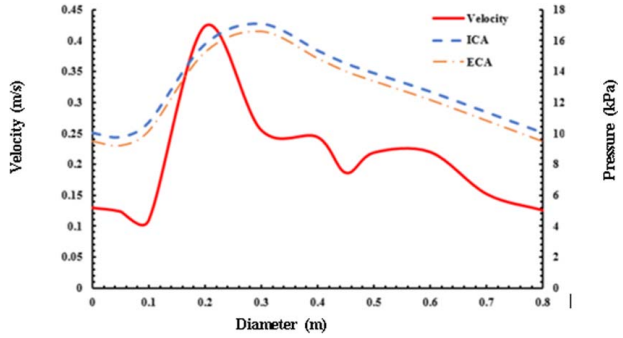

Fig. 11 Plot of the unsteady inlet velocity waveform and resultant Windkessel outlet waveforms

analyses for pulsatile flow in the carotid bifurcation artery geometry used to develop the 3-D printed mock arterial vessel model. The following sections present the results for this work.

3.1 3-D Printed Test Sample Particle Image Velocimetry Results and Validation. This section presents the results for the transient flow experiment run on the test sample (the initial square extrusion test sample). As mentioned previously, a MATLAB script was developed to obtain the Womersley velocity profile solution at the same given time interval in the velocity waveform that the PIV result was obtained. A plot of the Womersley velocity profile solution is provided in Fig. 12. From Fig. 12, it appears that the PIV result reveals a Womersley profile that has a maximum velocity magnitude that is similar to the Womersley velocity profile solution. The maximum velocity in the PIV result is 0.34 m/s and the maximum velocity in the Womersley solution profile is 0.37 m/s. The PIV result is within 97% in agreement with the Womersley solution when comparing the maximum velocity. However, there is a significant difference in the flow profile trend from wall to wall when comparing both the PIV and numerical Womersley solution.

The Womersley numerical velocity profile solution is nonparabolic and indicates that the flow is inertia dominant. The PIV result shows that the velocity profile is highly skewed toward the upper wall. This could be attributed to the pulsatile pressure wave and high centrifugal forces caused by the curves and bends in the tubing that delivers fluid from the pump to the test section. The no-slip condition is also not captured on the wall of the test sample. There is also little to no flow tracer particle adhesion on the vessel wall which leads us to believe that the inability of capturing the no-slip condition could be attributed to light scattering from the laser to the fluorescent particles and blurring at the wall.

3.2 Arterial Model Particle Image Velocimetry Analysis and Computational Fluid Dynamics Results. As mentioned previously, the same pulsatile flow loop used in the transient initial

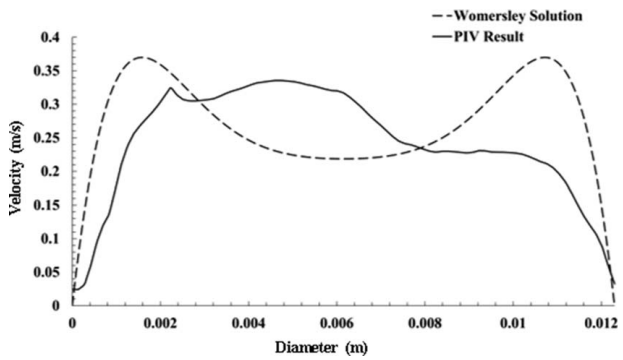

Fig. 12 Plot of the Womersley solution velocity profile and the PIV velocity profile at 5.8 s in the sinusoidal velocity waveform

Downloaded from http://heattransfer.asmedigitalcollection.asme.org/openengineering/article-pdf/doi/10.1115/1.4056639/6977727/aoje_2_021010.pdf by guest on 19 July 2024

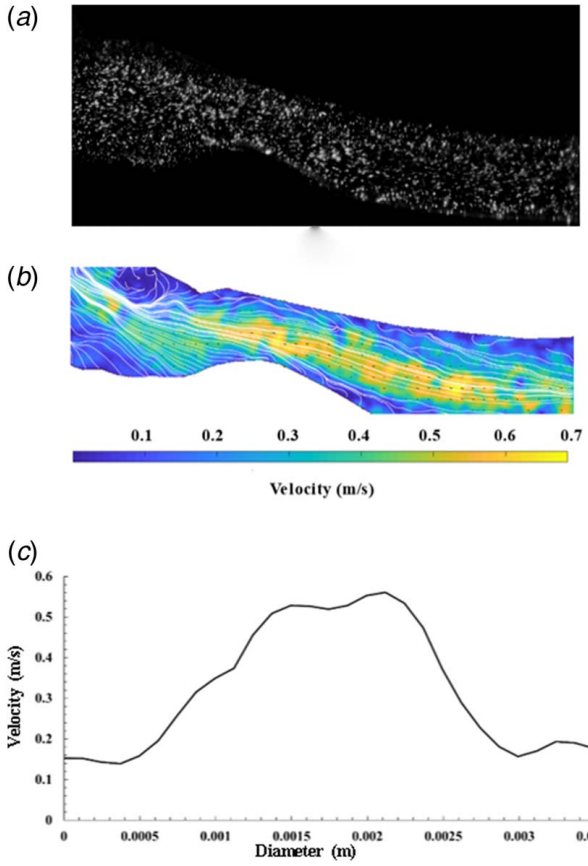

Fig. 13 Carotid artery transient PIV results: (*a*) raw PIV image, (*b*) velocity vector field, contour, and streamlines, and (*c*) extracted velocity profile at the center of the ROI

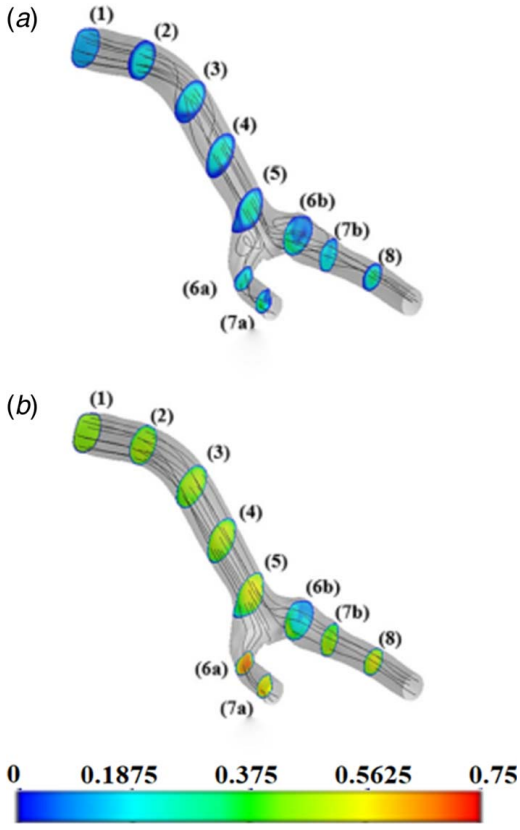

Fig. 14 Contour plots of velocity and streamline traces of flow during (*a*) diastole and (*b*) systole (fifth cardiac cycle $t = 5.2$ s)

square extrusion test sample experiments was used for transient experimental PIV analysis of the 3-D printed arterial mock vessel. For experimental PIV analysis, the flow loop was run over a period of 5 min prior to collecting data to ensure that the system transients (bubbles and other startup-unsteady flow effects) present in the arterial model section were minimized/removed. The pump and PIV system were synchronized to record data in time with the periodicity of the pulsatile waveform. Figure 13(*a*) presents the raw PIV image, Fig. 13(*b*) presents the velocity vector field and streamlines, and Fig. 13(*c*) presents the velocity profile that was obtained from the transient mock arterial vessel experiment. As shown in Fig. 13(*b*), the highest velocity magnitude occurs at the stenosis section and continues throughout the branch of the ICA. The high magnitude of velocity occurs due to the Venturi effect caused by the restriction at the stenosis (ROI). The continuation of this trend occurs due to the varying diameter along the ICA branch centerline.

The streamlines shown in Fig. 13(*b*) demonstrate areas of strong unsteadiness. Figure 13(*b*) also shows vortex shedding at the sinus bulb and recirculation upstream of the stenosis near the wall. As shown in the extracted velocity profile at the ROI in Fig. 13(*c*), the no-slip condition is not captured/observed. This is partially attributed to the varying curvature, scattering of light, and the varying plane along the axis of both the ICA and ECA branch centerline.

For CFD simulations, the CFD simulations were run over a period of 5 s (five cardiac waveforms) before retrieving computational data at systole and diastole in the cardiac waveform. The characteristic profile inside the carotid bifurcation artery is shown in Fig. 14 for both systole (5.2 s) and diastole (5.8 s) during cycle 5 of the cardiac flow waveform. Contours of axial velocities have been plotted along eight sliced planes normal to the direction of flow in Fig. 14. Flow streamlines representing the fluid flow trajectory are tracked and superimposed on the transparent mesh and the axial velocity contours. As depicted in slice 3 in Fig. 14 of both diastole and systole, a Womersley flow profile is established upstream of the sinus bulb region of slice 3 and continues throughout the artery for both cases in the cardiac cycle observed. During diastole the flow is highly skewed toward the wall as shown in each axial velocity contour. The streamlines are also disorganized in the common carotid artery (CCA) region and show areas of flow separations and secondary flow upstream of the internal and external carotid artery (ICA and ECA). The velocity profile at the stenosed region is extracted from the same location where the PIV velocity profile was extracted in the mock arterial PIV flow experiments. Similar to the PIV experiment results, the CFD velocity profile is asymmetric.

The asymmetric flow pattern plainly depicts strong unsteadiness (not to be confused with turbulence as the Reynolds number is $\mathrm{Re} = 545$) downstream of the sinus, while the remaining flow dampens upstream of the sinus region. During diastole, fewer velocity profiles appear to have a Womersley profile and the streamlines are much more organized. This is believed to be due to the large momentum increase of fluid motion from systole to diastole in which the flow has achieved maximum flow. The sinus bulb region remains to have a Womersley profile which indicates that possibly some recirculating flow occurs in this region. Similar findings have also been reported, whereby such skewed flow structure is primarily caused by the misalignment of the mean axis of the artery, curvature of the lumen, and unsteady centrifugal forces caused by the sudden decrease and increase in flow velocity [35–37].

Figure 15 shows a plot of the CFD velocity profile solution extracted at systole and the PIV result that was also obtained during systole. The plots are very similar when comparing the maximum velocity in the profiles. The CFD result has a maximum velocity of 0.6 m/s, whereas the PIV result has a maximum velocity of 0.55 m/s. The maximum velocity of the

Downloaded from http://heattransfer.asmedigitalcollection.asme.org/openengineering/article-pdf/doi/10.1115/1.4056639/6977727/aoje_2_021010.pdf by guest on 19 July 2024

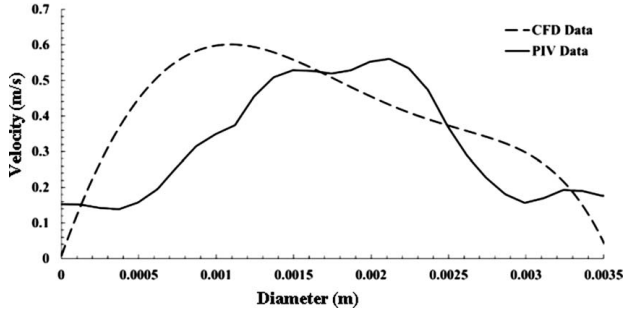

Fig. 15 CFD and PIV velocity profiles extracted at the ROI site at $t = 5.2$ s in the cardiac cycle

PIV result has a 92% agreement with the CFD maximum velocity result. The major difference is the trend in the profiles and the absence of the no-slip condition in the PIV velocity profile result. Similar to the straight pipe PIV experiment, the absence of the no-slip condition in the PIV result could again be attributed to the glaring of the laser light sheet, curves and bends present in the flow loop, and additional factors such as the misalignment of the mean axis of the artery, bends and curvature of the walls [38–41], and unsteady centrifugal forces as mentioned in the CFD case.

Overall, the developed 3-D printed anatomical models appear to be a good baseline procedure for developing anatomical mock vessel models for PIV analyses. Several characteristics of the arterial model presented in this work complicate traditional fabrication approaches (e.g., using CNC milling): (1) both the ICA and ECA branches are curved in the anteroposterior direction and (2) the vessel cross-sections are constantly varying in diameter along the centerline axis. Indeed, initial attempts revealed that fabricating the model out of acrylic would require splitting the model into two halves to machine the internal surface of the vein lumen and then fusing the two halves together. The seam created by this procedure restricts the laser light sheet and camera access.

Additionally, because of the curvature of the arterial model, a four-axis CNC mill would be required to accurately reproduce the model geometry, greatly increasing the cost of fabrication. The direct 3-D printing approach presented herein overcomes these limitations. However, further work is needed to rectify the issues of the absence of the no-slip condition and possible flow loop system added unsteady and transient effects when retrieving and analyzing PIV results.

4 Conclusion

The aim of this work was to introduce a novel approach for producing optically clear 3-D printed rigid anatomical arterial models that are suitable for PIV analysis using a common 3-D inkjet printing process. PIV analyses were conducted on a straight pipe sample and a 3-D printed mock vessel installed in a complex transient flow loop to assess flow profiles and the clarity of the model. A CFD simulation was also conducted on the same carotid bifurcation artery geometry, and the results were used as a benchmark comparison for PIV results. The main limitations of the rapid prototyping of 3-D printed rigid arterial vessel models as described herein are the need to manually post-process vessel models via soaking, wet sanding, polishing the inner and outer surfaces of the anatomical vessels, and some issues with producing highly resolved velocity vectors near the walls for unsteady flow during PIV data post-processing.

Despite these limitations, the approach described in the present work for fabricating complex optically clear arterial models is well suited for PIV measurements. Future work should include measuring the surface roughness of the interior of the arterial models and possibly exploring the use of techniques such as vapor deposition smoothing [23] to rectify high surface roughness which could promote glaring and undesired frictional energy losses. Future work should also involve performing PIV uncertainty analyses and exploring further post-processing techniques to rectify optical clarity and reduce errors in PIV measurements and post-processing. The results obtained in this work show excellent promise for using the developed approach for developing 3-D printed anatomical models for experimental PIV analyses.

Acknowledgment

The authors would like to acknowledge Johanna Okerlund with the University of North Carolina at Charlotte Makerspace Center for providing training and guidance on 3-D printing vessels using the Form Labs 2 3-D printer. The authors would also like to thank Associate Professor Dr. Wesley Williams of the UNC-C Department of Engineering Technology and Construction Management (ETCM) for his advice and support on 3-D printing the models presented in this work.

Funding Data

- This research was funded by the University of North Carolina at Charlotte Faculty Research Grant (FRG) and the NC Space Grant New Investigator Award through the National Aeronautical Space Administration (NASA).

Conflict of Interest

There are no conflicts of interest.

Data Availability Statement

This article does not include research in which human participants were involved. Informed consent not applicable. This article does not include any research in which animal participants were involved. The datasets generated and supporting the findings of this article are obtainable from the corresponding author upon reasonable request.

Nomenclature

i = imaginary number
r = indexed radius
t = time
u = axial velocity
C = compliance for large arteries and arterioles
P = pressure
R = radius value
u_{ave} = average flow velocity
J_0 = Bessel function of zero order
R_d = distal resistance for large arteries and arterioles
R_p = proximal resistance for large arteries and arterioles
Re = Real result
α = the Womersley number
μ = dynamic viscosity
ω = frequency
ρ = density

References

[1] Kelly, B. B., Narula, J., and Fuster, V., 2012, "Recognizing Global Burden of Cardiovascular Disease and Related Chronic Disease," MT Sinai J. Med., **79**(6), pp. 632–640.
[2] Cloonan, A. J., Shahmirzadi, D., Li, R. X., Doyle, B. J., Konofagou, E. E., and McGloughlin, T. M., 2014, "3D-Printed Tissue-Mimicking Phantoms for Medical Imaging and Computational Validation Applications," 3D Print Addit. Manuf., **1**(1), pp. 14–23.
[3] Cardiovascular Diseases (CVDs), https://www.who.int/en/news-room/fact-sheets/detail/cardiovascular diseases-(cvds), Accessed July 10, 2022.

Downloaded from http://heattransfer.asmedigitalcollection.asme.org/openengineering/article-pdf/doi/10.1115/1.4056639/6977727/aoje_2_021010.pdf by guest on 19 July 2024

[4] Aryan, H., Beigzadeh, B., and Siavashi, M., 2022, "Euler–Lagrange Numerical Simulation of Improved Magnetic Drug Delivery in a Three-Dimensional CT-Based Carotid Artery Bifurcation," Comput. Methods Programs Biomed., **219**, 106778.
[5] Gates, P. E., Gurung, A., Mazzaro, L., Aizawa, K., Elyas, S., Strain, W. D., Shore, A. C., and Shandas, R., 2018, "Measurement of Wall Shear Stress Exerted by Flowing Blood in the Human Carotid Artery: Ultrasound Doppler Velocimetry and Echo Particle Image Velocimetry," Ultrasound Med. Biol., **44**(7), pp. 1392–1401.
[6] Hewlin, Jr., R. L., and Kizito, J., 2018, "Development of an Experimental and Digital Cardiovascular Arterial Model for Transient Hemodynamic and Postural Change Studies: A Preliminary Analysis," Cardiovasc. Eng. Technol., **9**(1), pp. 1–31.
[7] Shintani, Y., Lino, K., Yamamoto, Y., Kato, H., Takemura, H., and Kiwata, T., 2018, "Analysis of Computational Fluid Dynamics and Particle Image Velocimetry Models of Distal-End Side-to-Side and End-to-Side Anastomoses for Coronary Artery Bypass Grafting in Pulsatile Flow," Circul. J., **82**(1), pp. 110–117.
[8] Mokhtar, N. H., Abas, A., Razak, N. A., Hamid, M. N. A., and Teong, S. L., 2017, "Effect of Different Stent Configurations Using Lattice Boltzmann Method and Particles Image Velocimetry on Artery Bifurcation Aneurysm Problem," J. Theor. Biol., **433**, pp. 73–84.
[9] McGloughlin, T. M., and Doyle, B. J., 2010, "New Approaches to Abdominal Aortic Aneurysm Rupture Risk Assessment: Engineering Insights With Clinical Gain," Arterioscler. Throm. Vasc. Biol., **30**(9), pp. 1687–1694.
[10] Ha, H., and Lee, S. J., 2014, "Effect of Swirling Inlet Condition on the Flow Field in a Stenosed Arterial Vessel Model," Med. Eng. Phys., **36**(1), pp. 119–128.
[11] Bluestein, D., Niu, L., Schoephoerster, R. T., and Dewanjee, M. K., 1997, "Fluid Mechanics of Arterial Stenosis: Relationship to the Development of Mural Thrombus," Ann. Biomed. Eng., **25**(2), pp. 344–356.
[12] Doyle, B. J., Cloonan, A. J., Walsh, M. T., Vorp, D. A., and McGloughlin, T. M., 2010, "Identification of Rupture Locations in Patient-Specific Abdominal Aortic Aneurysms Using Experimental and Computational Techniques," J. Biomech., **43**(7), pp. 1408–1416.
[13] Winkler, C. M., Kuhn, A. I., Hentschel, G., and Glasmacher, B., 2022, "A Review on Novel Channel Materials for Particle Image Velocimetry Measurements—Usability of Hydrogels in Cardiovascular Applications," Gels, **8**(502), pp. 1–17.
[14] Stoiber, M., Schloglhofer, T., Aigner, P., Grasl, C., and Schima, H., 2013, "An Alternative Method to Create Highly Transparent Hollow Models for Flow Visualization," Int. J. Artif. Organs, **36**(2), pp. 131–134.
[15] Nguyen, T. T., Biadillah, Y., Mongrain, R., Brunette, J., Tardif, J.-C., and Bertrand, O. F., 2004, "A Method for Matching the Refractive Index and Kinematic Viscosity of a Blood Analog for Flow Visualization in Hydraulic Cardiovascular Models," ASME J. Biomech. Eng., **126**(4), pp. 529–535.
[16] Yip, R., Mongrain, A., Ranga, J., et al., 2004, "Development of Anatomically Correct Mock-Ups of the Aorta for PIV Investigations," Canadian Design Engineering Network CDEN Conference, Montreal, Canada.
[17] Yazdi, S. G., Geoghegan, P. H., Docherty, P. D., Jermy, M., and Khanafer, A., 2018, "A Review of Arterial Phantom Fabrication Methods for Flow Measurement Using PIV Techniques," Ann. Biomed. Eng., **46**(11), pp. 1697–1721.
[18] Arcaute, K., and Wicker, R. B., 2008, "Patient-Specific Compliant Vessel Manufacturing Using Dip-Spin Coating of Rapid Prototyped Molds," ASME J. Manuf. Sci. Eng., **130**(5), p. 051008.
[19] Allard, L., Soulez, G., Chayer, B., Treyve, F., Qin, Z., and Cloutier, G., 2009, "Multimodality Vascular Imaging Phantoms: A New Material for the Fabrication of Realistic 3D Vessel Geometries," Med. Phys., **36**(8), pp. 3758–3763.
[20] Song, M. S., Choi, H. Y., Seong, J. H., and Kim, E. S., 2014, "Matching-Index-of-Refraction of Transparent 3D Printing Models for Flow Visualization," Nucl. Eng. Des., **284**, pp. 185–191.
[21] Hopkins, L. M., Kelly, J. T., Wexler, A. K., and Prasad, A. K., 2000, "Particle Image Velocimetry Measurements in Complex Geometries," Exp. Fluids, **29**(1), pp. 91–95.
[22] Yousif, M. Y., Holdsworth, D. W., and Poepping, T. L., 2009, "Deriving a Blood-Mimicking Fluid for Particle Image Velocimetry in Sylgard-184 Vascular Models," Annual International Conference of the IEEE Engineering in Medicine and Biology Society, pp. 1412–1415, PMID: 19964526, .
[23] Lai, S. S., Yiu, B. Y., Poon, A. K., et al., 2009, "Design of Anthropomorphic Flow Phantoms Based on Rapid Prototyping of Compliant Vessel Geometries," UMB, **39**(9), pp. 1654–1664.
[24] Ruedinger, K. L., Medero, R., and Roldan-Alzate, A., 2019, "Fabrication of Low-Cost Patient-Specific Vascular Models for Particle Image Velocimetry," Cardiovasc. Eng. Technol., **10**(3), pp. 500–507.
[25] Laughlin, M. E., Stephens, S. E., Hestekin, J. A., and Jensen, M. O., 2022, "Development of Custom Wall-Less Cardiovascular Flow Phantoms With Tissue-Mimicking Gel," Cardiovasc. Eng. Technol., **13**(1), pp. 1–13.
[26] Ho, W. H., Tshimanga, I. J., Ngoepe, M. N., Jermy, M. C., and Geoghegan, P. H., 2022, "Evaluation of a Desktop 3D Printed Rigid Refractive-Indexed-Matched Flow Phantom for PIV Measurements on Cerebral Aneurysms," Cardiovasc. Eng. Technol., **11**(1), pp. 14–23.
[27] Formlabs Community Forum (Index of Refraction), https://forum.formlabs.com/t/whats-the-index-of-refraction-of-the-clear-resin/9541, 2018.
[28] Womersley, J. R., 1955, "Method for the Calculation of Velocity, Rate of Flow, and Viscous Drag in Arteries When the Pressure Gradient Is Unknown," J. Physiol., **127**(3), pp. 553–563.
[29] Sexl, T., 1930, "Uber den Von E.G., Richardson Entdeckten Annulare Effekt," Z. Phys., **61**(5–6), pp. 349–362.
[30] Hewlin, Jr., R. L., Ciero, A., and Kizito, J. P., 2019, "Development of a Two-Way Coupled Eulerian–Lagrangian Computational Magnetic Nanoparticle Targeting Model for Pulsatile Flow in a Patient-Specific Diseased Left Carotid Bifurcation Artery," J. Cardiovasc. Eng. Technol., **12**(1), pp. 1–15.
[31] Hewlin, Jr., R. L., and Kizito, J. P., 2013, "Comparison of Carotid Bifurcation Hemodynamics in Patient-Specific Geometries at Rest and During Exercise," ASME 2013 Fluids Engineering Division Summer Meeting, Incline Village, NV, July 7–11.
[32] Stanley, N., Ciero, A., Timms, W., and Hewlin, Jr., R. L., 2019, "Development of 3-D Printed Optically Clear Rigid Anatomical Vessels for Particle Image Velocimetry Analysis in Cardiovascular Flow," ASME 2019 International Mechanical Engineering Congress and Exposition, Salt Lake City, UT, Nov. 11–14.
[33] Hewlin, Jr., R. L., and Kizito, J. P., 2017, "Development of an Experimental and Digital Cardiovascular Arterial Model for Transient Hemodynamic and Postural Change Studies: "A Preliminary Framework Analysis"," J. Cardiovasc. Eng. Technol., **8**(32), pp. 1–31.
[34] Hewlin, Jr., R. L., Smith, M., and Kizito, J. P., 2022, "Computational Assessment of Unsteady Flow Effects on Magnetic Nanoparticle Targeting Efficiency in a Magnetic Stented Carotid Bifurcation Artery," J Cardiovasc. Eng. Technol., in review.
[35] Buchmann, N. A., Atkinson, C., Jeremy, M. C., and Soria, J., 2011, "Tomographic Partical Image Velocimetry Investigation of the Flow in a Modeleld Human Carotid Artery Bifurcation," Exp. Fluids, **50**(4), pp. 1131–1151.
[36] Chen, H., Ebner, A. D., Rosengart, A. J., Kaminski, M. D., and Ritter, J. A., 2004, "Analysis of Magnetic Drug Carrier Particle Capture by a Magnetizable Intravascular Stent: 1. Parametric Study With Single Wire Correlation," J. Magn. Magn. Mater., **284**, pp. 181–194.
[37] Vetel, J., Garon, A., and Pelletier, D., 2009, "Lagrangian Coherent Structures in the Human Carotid Artery Bifurcation," Exp. Fluids, **46**(6), pp. 1067–1079.
[38] Williams, H. C., Hubbell, C. W., and Frenkell, G. H., 1902, "Experiments at Detroit, MI, on the Effect of Curvature Upon the Flow of Water in Pipes," Trans. Am. Soc. Civil Eng., **47**(1), pp. 1–196.
[39] Eustice, J., 1911, "Experiments of Streamline Motion in Curved Pipes," Proc. R. Soc. A: Math. Phys. Eng. Sci., **85**, pp. 119–131.
[40] Eustice, J., 1910, "Flow of Water in Curved Pipes," Proc. R. Soc. A: Math. Phys. Eng. Sci., **84**, pp. 107–118.
[41] Berger, S. A., Talbot, L., and Yao, L. S., 1983, "Flow in Curved Pipes," Ann. Rev. Fluid Mech., **15**(1), pp. 461–512.
[42] Gharahi, H. B., Zambrano, B., Zhu, E., et al., 2016, "Computational Fluid Dynamic Simulation of Human Carotid Artery Bifurcation Based on Anatomy and Volumetric Blood Flow Rate Measured With Magnetic Resonance Imaging," Int. J. Adv. Eng. Sci., **8**(1), pp. 40–60.

Downloaded from http://heattransfer.asmedigitalcollection.asme.org/openengineering/article-pdf/doi/10.1115/1.4056639/6977727/aoje_2_021010.pdf by guest on 19 July 2024